Theoretical examination of stress fields in $Pb(Zr_{0.5}Ti_{0.5})O_3$

Nicholas J. Ramer,* E. J. Mele†,‡ and Andrew M. Rappe*,‡
*Department of Chemistry, †Department of Physics and
‡Laboratory for Research on the Structure of Matter
University of Pennsylvania, Philadelphia, PA 19104
(July 27, 1999)

In this paper, we develop a rigorous formulation of the local stress field. This approach can be used in conjunction with any first-principles method to study stress fields in complex bonded systems. In particular we investigate the induced stress fields resulting from the homogeneous deformations of tetragonal $PbTiO_3$ and rhombohedral $PbZrO_3$. As an extension of these findings we also compute the induced stress fields resulting from homogeneous deformation of the (100) and (111) orderings of $Pb(Zr_{0.5}Ti_{0.5})O_3$. The stress-field responses in these four materials are compared and their piezoelectric responses are discussed.
PACS numbers: 77.65.L, 77.84.Dy, 77.65.-j, 71.15.Mb, 31.15.Ar

Keywords: piezoelectricity, stress field, $PbTiO_3$, $PbZrO_3$, PZT, (100)-$Pb(Zr_{0.5}Ti_{0.5})O_3$, (111)-$Pb(Zr_{0.5}Ti_{0.5})O_3$

I. INTRODUCTION

When mechanical stress is applied to a piezoelectric material, microscopic atomic rearrangements occur which give rise to a change in the macroscopic electric polarization of the material. Conversely, application of a voltage across a piezoelectric material produces an internal strain within it. In either case, it is the material's internal structural behavior (and therefore spontaneous polarization) under applied or induced stress that underlies the piezoelectric response.

The ability of piezoelectric materials to interconvert electrical and mechanical energy lies at the foundation of many electro-optic and electro-acoustic devices. The use of piezoelectric materials in these devices stems from the need to monitor the magnitude of induced or applied electrical response through the device. One of the clearest examples of such an application is seen in the constant tunneling voltage mode of the scanning-tunneling microscope (STM).[1] Piezoelectric materials also play a vital role in electro-acoustic transducers. In these devices the piezoelectric material acts as an interpreter for the incoming (or outgoing) sound wave and the outgoing (or incoming) electric signal. These types of devices have uses in underwater and medical ultrasonic imaging.

In this paper, we present a first-principles investigation of the distorted perovskite materials $PbTiO_3$ and $PbZrO_3$ at zero temperature and study the spatial variation of their stress-field responses to an externally applied uniform strain. In addition, stress-field studies of the (100) and (111) orderings of the solid solution $Pb(Zr_{0.5}Ti_{0.5})O_3$ (PZT) are also reported. Our selection of PZT is motivated by the wealth of experimental studies characterizing the strong piezoelectric response in various composite PZT ceramics.[2] In Section II we briefly describe the formalism for construction of the local stress fields. In Section III we present results for the computation of local stress fields induced by a uniform uniaxial deformation. A discussion of the local stress fields produced in the simple perovskite crystals and the more complex PZT superlattices is provided in Section IV and we conclude the paper in Section V.

II. STRESS-FIELD FORMALISM

It is central to the study of any piezoelectric crystal to understand the material's internal response to an externally applied strain. Experimentally, a particular crystal's structural response to an applied strain can be measured using various diffraction techniques[3] or direct measurement of the changes in the dimension of the sample by electrical capacitance or optical interference.[4] In order to ascertain the effect strain has upon piezoelectric response, these techniques are paired with high-field measurement of strain hysteresis and polarization change. More recently, field-induced strain has been measured using a displacement magnification technique.[5] However because the formation and testing of many of these strained materials is complicated and possibly destructive,[6] it is advantageous to have a concise theoretical method from which information concerning the microscopic response of a system to an external strain can be extracted.

We consider the response of a system to a homogeneous long wavelength deformation (scaling transformations describing pure dilation, strain or shear). For an interacting system of atoms, the introduction of any of these uniform deformations can induce a force distribution on all the structural degrees of freedom of the unit cell. Within a harmonic theory, the induced atomic force distribution, $\vec{F}$, contains all the relevant information about the redistribution of the external stress within the cell. Therefore, the starting point for the computation of the local stress fields is the calculation of the induced force distribution. This can be accomplished using local density functional theory. These theoretical methods have proven to be very successful for studying structural phenomena in a broad class of condensed phases. Below we outline our method to compute the stress field given the local force density. Once the stress field has been constructed, correlations between the elastic response and the structural features of the system can be made. A more detailed explanation of the method will be presented elsewhere.[7]

We begin with the principle of virtual work in the presence of an induced force distribution $\vec{F}_m$. Any set of displacements of the nuclear coordinates $\vec{u}$ for a particular interacting system produces a variation of the energy, U, according to

$$\delta U = \sum_{m=1}^{N_a} \vec{F}_m \cdot \vec{u}_m \tag{1}$$

where m represents the m-th ion of the interacting system. It is useful to convert the displacements and forces to continuous fields:

$$\begin{aligned} \delta U &= \frac{1}{\Omega} \int_{\text{cell}} d^3 r \vec{F}\left(\vec{r}\right) \cdot \vec{u}\left(\vec{r}\right) \\ &= \sum_{\vec{G}} \vec{F}\left(-\vec{G}\right) \cdot \vec{u}\left(\vec{G}\right) \end{aligned} \tag{2}$$

In the last line we have used lattice translational symmetry to transform the force and displacement distributions to a reciprocal space representation. The principle of virtual work can be recast in terms of the internal strains in the structure

$$\begin{aligned} \delta U &= \int_{\text{cell}} d^3 r \overrightarrow{\overrightarrow{\sigma}}\left(\vec{r}\right) \cdot \overrightarrow{\overrightarrow{\epsilon}}\left(\vec{r}\right) \\ &= \Omega \sum_{\vec{G}} \overrightarrow{\overrightarrow{\sigma}}\left(-\vec{G}\right) \cdot \overrightarrow{\overrightarrow{\epsilon}}\left(\vec{G}\right) \end{aligned} \tag{3}$$

where $\overrightarrow{\overrightarrow{\sigma}}$ is the 6-component stress field tensor and $\overrightarrow{\overrightarrow{\epsilon}}$ is the 6-component strain tensor. (Since only the contraction of two rank-2 tensors is required in equation (3), the tensors are represented as length-6 vectors for simplicity.)

The direct space components of the strain tensor can be directly related to the displacement field,

$$\epsilon_n\left(\vec{r}\right) = \vec{\nabla} \cdot \Gamma_n \cdot \vec{u}\left(\vec{r}\right) \tag{4}$$

where ϵ_n is the n-th component of the strain tensor ($n = 1, \ldots, 6$) and Γ_n is the 3×3 matrix determining the symmetry of ϵ_n. Transforming this relationship into Fourier space gives the particularly convenient result

$$\epsilon_n\left(\vec{G}\right) = \vec{G} \cdot \Gamma_n \cdot \vec{u}\left(\vec{G}\right) \tag{5}$$

Combining equation (5) for all 6 components of the strain tensor gives

$$\overrightarrow{\overrightarrow{\epsilon}}\left(\vec{G}\right) = \mathcal{P} \cdot \vec{u}\left(\vec{G}\right) \tag{6}$$

or

$$\mathcal{P}^{-1} \cdot \overrightarrow{\overrightarrow{\epsilon}}\left(\vec{G}\right) = \vec{u}\left(\vec{G}\right) \tag{7}$$

Inserting this relationship into the last line of equation (2) and equating lines (2) and (3) yields

$$\delta U = \Omega \sum_{\vec{G}} \vec{F}\left(-\vec{G}\right) \cdot \mathcal{P}^{-1} \cdot \overrightarrow{\overrightarrow{\epsilon}}\left(\vec{G}\right) \tag{8}$$

$$= \Omega \sum_{\vec{G}} \overrightarrow{\overrightarrow{\sigma}}\left(-\vec{G}\right) \cdot \overrightarrow{\overrightarrow{\epsilon}}\left(\vec{G}\right) \tag{9}$$

Equating the arguments of the summations in equations (8) and (9) yields all 6 components of the local stress field in reciprocal space:

$$\overrightarrow{\overrightarrow{\sigma}}\left(-\vec{G}\right) = \vec{F}\left(-\vec{G}\right) \cdot \mathcal{P}^{-1} \tag{10}$$

By transforming according to

$$\overrightarrow{\overrightarrow{\sigma}}\left(\vec{r}\right) = \sum_{\vec{G}} \overrightarrow{\overrightarrow{\sigma}}\left(\vec{G}\right) e^{i\vec{G}\cdot\vec{r}} \tag{11}$$

we can construct the stress distribution in direct space, and this result can be used to generate a map of the spatial distribution of the n-th stress field of the system.

Vanderbilt[8] has correctly pointed out that this formalism only enables computation of the stress-field components which possess the periodicity of the unit cell. In addition the $\vec{G}$=0 stress tensor can be computed by the approach of Nielsen and Martin.[9,10] Development of a method for the computation of the stress-field components which are uniform in one or two dimensions and of finite wavelength in the others is in progress.

III. RESULTS

The first-principles calculations presented in this paper are performed within density functional theory,[11] and the local density approximation (LDA) is used to describe the electron-electron interactions. For the solid-state calculations, the single electron wave functions are expanded in a plane-wave basis using a cutoff energy of 50 Ry.

To describe the electron-nuclear interaction, optimized pseudopotentials[12] in fully separable nonlocal form[13] are used. An additional feature of our nonlocal pseudopotentials[14] is their improved transferability over a wide range of electronic configurations. We have been able to exploit the flexibility contained in the separation of the local and non-local parts of the pseudopotential. By designing the form of the local potential so that the pseudo-eigenvalues and all-electron eigenvalues agree at an additional charge state, it is possible to improve the transferability of the potential across the charge states lying between the original reference state and this second charge state.

Due to the need for high accuracy when examining ferroelectric phenomena, semi-core shells are included in the generation of the pseudopotentials. We include as valence states the $3s$ and $3p$ for Ti and the $4s$ and $4p$ for Zr. The $5d$ shell is included for Pb. Furthermore, scalar relativistic effects are included in the generation of the Pb pseudopotential.[15] For each metal, a pseudopotential is constructed using a designed local potential with the addition of a square well within the core region. By doing so, we are able to achieve excellent transferability of the pseudopotential over a variety of charge and excited states. For each of the metals, excellent agreement of the pseudo-eigenvalues and total energy differences with the all-electron results is achieved for charge states of +4 to neutral. The oxygen pseudopotential is constructed using the s angular momentum channel as the local potential.

Brillouin zone integrations for $PbTiO_3$ and $PbZrO_3$ were done using a $4 \times 4 \times 4$ Monkhorst-Pack k-point mesh.[16] It should be noted that to compute the nonuniform force distribution resulting from the application of a uniform external

TABLE I. Computed and experimental equilibrium lattice constants and atomic positions for tetragonal $PbTiO_3$ and rhombohedral $PbZrO_3$.

	Present	Theory	Experiment
		$PbTiO_3$	
a(Å)	3.870	3.862[a]	3.905[b]
c/a	1.063	1.054	1.063
z(Ti)	0.531	0.537	0.540
z(O_1,O_2)	0.604	0.611	0.612
z(O_3)	0.098	0.100	0.112
		$PbZrO_3$	
c(Å)	4.143	4.12[c]	
z(Zr)	0.540	0.545	
x, y(O_1)	0.583	0.590	
z(O_1)	0.057	0.061	

[a]Reference[21].
[b]Reference[22].
[c]Reference[23].

stress, additional k-points were needed due to the broken symmetries in the distorted structure.

The calculations involving the rhombohedral $PbZrO_3$ and (111)-PZT deserve closer consideration. Crystallographically, the zero-temperature form of $PbZrO_3$ is orthorhombic with 40 atoms per unit cell.[17–19] In order to simplify our comparisons of the local stress fields, the structure of $PbZrO_3$ was fully relaxed within the rhombohedral symmetry of zero-temperature ferroelectric phase of $PbZrO_3$ with small Ti doping.[2] Rhombohedral strains of the unit cell shape away from cubic were neglected since they have been shown to be quite small ($\sim 0.1^\circ$).[20] In the case of (111)-PZT, rhombohedral strains were also neglected to simplify analysis of the induced local stress fields.

As part of the local stress-field calculations, complete structural relaxations of both internal coordinates and crystal lattice constants were completed for the $PbTiO_3$ and $PbZrO_3$ distorted perovskite structures. We report our atomic positions and lattice constants for tetragonal $PbTiO_3$ and rhombohedral $PbZrO_3$ in Table I and compare these results with previous theoretical and experimental values where possible. The absence of experimental values for the rhombohedral $PbZrO_3$ is explained by our simplification of the $PbZrO_3$ structure as described above. In the case of $PbTiO_3$, our agreement with previously reported theoretical[21] and experimental results[22] is quite good and is within the error expected from density functional solid-state calculations done within LDA. For the rhombohedral $PbZrO_3$, our results agree quite well with the theoretical results of Singh.[23] (In Singh's work, the lattice constant of rhombohedral $PbZrO_3$ was not relaxed. The theoretically determined lattice constant of the high temperature cubic perovskite was used instead.)

TABLE II. Computed equilibrium lattice constants and atomic positions for tetragonal (100)-PZT and rhombohedral (111)-PZT. Experimental lattice constants are given for randomly ordered PZT ceramics close to the 50-50 batch composition. See text for description.

	Present	Experiment
	(100)-Pb($Zr_{0.5}Ti_{0.5}$)O_3	
c(Å)	8.313	8.279[a]
c/a	2.083	2.053
z(Pb_2)	0.468	
z(Ti)	0.211	
z(Zr)	0.714	
z(O_1)	-0.049	
z(O_2,O_3)	0.185	
z(O_4)	0.424	
z(O_5,O_6)	0.660	
	(111)-Pb($Zr_{0.5}Ti_{0.5}$)O_3	
c(Å)	8.043	8.164*
z(Pb_2)	0.498	
z(Ti)	0.237	
z(Zr)	0.737	
x(O_1)	0.221	
z(O_1)	-0.014	
x(O_4)	0.721	
z(O_4)	0.470	

[a]Reference[2].

Atomic and lattice relaxations were also performed for the PZT superlattices. The experimental lattice constants as well as theoretical lattice constants and relaxed atomic positions are contained in Table II. Experimental values for the (100)-PZT ceramic are taken for the tetragonal 50-50 batch composition PZT ceramic according to Jaffe $et\ al.$ (ceramic **3** using the notation from reference [2]). The experimental values for the (111)-PZT ceramic are taken for a rhombohedral PZT ceramic close to the 50-50 batch composition (ceramic **5** using the notation from reference [2]).

We studied the induced local stress fields by calculating the internal force distribution induced by a uniform external strain. The force distribution is obtained from first-principles density functional theory within the LDA using the Hellmann-Feynman theorem.[24,25] Since our stress-field formalism relies on the fact that any deformation must not take the system beyond lowest order in gradients of the total energy, attention must be paid to the magnitude of the deformations. We have found that $\pm 0.2\%$ deformations in lattice lengths and $\pm 0.5^\circ$ in lattice angles are within the harmonic limit of the potential energy. Extension of this work beyond harmonic order is a promising direction for the study of recently discovered piezoelectric single crystals which exhibit large reversible strains.[26]

There are 6 homogeneous deformations which can be made

to any crystal: dilation having the symmetry of $x^2+y^2+z^2$, uniaxial strains—tetragonal with symmetry $2x^2-y^2-z^2$ and orthorhombic with y^2-z^2 symmetry, and elementary shear operations (xy, xz, and yz). Based on crystal symmetry considerations, certain homogeneous deformations are degenerate and can easily be constructed from the other deformations. For a crystal subjected to any of the 6 homogeneous deformations one finds a local $internal$ stress field in all 6 stress components. It is important to note that for a given deformation, the induced stress fields corresponding to the 5 other deformations must each integrate to zero over the entire unit cell.

For brevity, we only report the local stress fields induced by an applied tetragonal uniaxial stress. In particular we focus our discussion on the internal tetragonal and dilation stress-field responses induced by a tetragonal compression. We have omitted the dilation response stress fields for the $PbTiO_3$, $PbZrO_3$ and (100)-PZT because they are quite similar to their respective tetragonal responses.

To simplify the visualization of the stress fields, we have chosen to show only the regions of highest induced local stress. For a tetragonal response to a tetragonal compressive deformation, light blue regions correspond to prolate response (expansive along the axial direction but compressive along the equatorial directions) and pink regions correspond to oblate response (compressive along the axial direction but expansive along the equatorial directions). For a dilation response to a uniaxial compressive deformation, light blue isosurfaces correspond to regions in the unit cell undergoing compression in all directions and pink isosurfaces correspond to expansion in all directions.

A. Tetragonal $PbTiO_3$

Figure 1 shows the tetragonal local stress field produced in response to a uniaxial tetragonal deformation of the zero-temperature equilibrium structure of tetragonal $PbTiO_3$. The (100) lattice direction contains the Pb atoms at the lower left forward corner and upper left forward corners of the unit cell. We find the region of highest induced stress does not involve the Pb atoms but instead straddles the Ti atom and is oriented along the (100) direction. In the upper half of the TiO_6 octahedron lying along the (100) direction, there is an oblate response which would shift the Ti along the (100) direction toward the upper half of the octahedron. In addition to the oblate response, there is a prolate response in the lower half of the TiO_6 octahedron. The effect of these volume deformations would be to elongate the lower half of the oxygen octahedron while shortening the upper half. Finally, there is no significant stress-field response involving the oxygens lying equatorial to the Ti atom.

B. Rhombohedral $PbZrO_3$

Figure 2 shows the tetragonal local stress field produced in response to a uniaxial tetragonal deformation of the zero-temperature equilibrium structure of rhombohedral $PbZrO_3$. The (111) atomic distortion direction contains the Pb atoms at the lower left forward and upper right rear corners of the unit cell. In this stress field, as in the tetragonal field for $PbTiO_3$, there is pairing of oblate and prolate regions surrounding the central metal atom. However, there is a clear difference between the responses for the two crystals. The regions in the response for the $PbZrO_3$ lie along a composite of the (111) ferroelectric distortion direction and (100) uniaxial strain direction. The corresponding motion of the Zr is toward the upper half of the ZrO_6 octahedron, along this composite direction. In addition to the motion of the Zr atom, the O atoms lying axial to the Zr atom are moving in a direction opposing the Zr atom motion.

C. Tetragonal (100)-$Pb(Zr_{0.5}Ti_{0.5})O_3$

Figure 3 shows the tetragonal local stress field produced in response to a uniaxial tetragonal deformation of the zero-temperature equilibrium structure of tetragonal (100)-$Pb(Zr_{0.5}Ti_{0.5})O_3$. The (100) lattice direction contains the Pb atoms at the lower left forward corner and upper left forward corners of the unit cell. For this super-cell, an alternating pattern of oblate and prolate responses is found lying along the 4-fold rotation axis. As a result of our imposition of tetragonal symmetry, we find response in the (100)-PZT superlattice lying exclusively along the (100) direction indicating atomic motions purely in the (100) direction, similar to the tetragonal response for $PbTiO_3$. This combination of responses leads to Ti and Zr motions toward the lower halves of the octahedra. The axial O atoms show opposing motion to the Ti and Zr atoms.

D. Rhombohedral (111)-$Pb(Zr_{0.5}Ti_{0.5})O_3$

Figures 4 and 5 show the dilation and tetragonal local stress fields produced in response to a uniaxial tetragonal deformation of the zero-temperature equilibrium structure of rhombohedral (111)-$Pb(Zr_{0.5}Ti_{0.5})O_3$. The (111) atomic distortion direction contains the Pb atoms at the lower left forward and upper right rear corners of the unit cell. The (100) lattice direction contains the Pb atom at the lower left forward and upper left forward corners of the unit cell. There are two crystallographically unique Pb atoms lying along the (111) direction in addition to the Ti and Zr atoms.

Dilation Response: Each individual region of highest induced stress field in the response is oriented perpendicular to the (111) atomic distortion direction. Unlike the responses for the previously mentioned crystals, we find the Ti and Zr atoms of (111)-PZT have negligible involvement. Instead we report alternating expansion and compression regions consisting of entire Pb_2O_4 octahedra. These octahedra are comprised of two adjacent Pb atoms lying along the (100) lattice direction and 4 equatorial O atoms. The overall pattern of the expansions and compressions shows the (111) stacking of the entire superlattice. Focusing on the Pb at the lower left forward corner, we find expansion of the Pb_2O_4 octahedron above this atom and contraction of the Pb_2O_4 octahedron below, resulting in largely downward motion of this Pb atom. Analogous reasoning shows that the dilation stress field causes upward motion of the central Pb atom. The expansion and contraction of the Pb_2O_4 octahedra also gives rise to equatorial oxygen motion in the (100) plane. The O atoms not involved in the Pb_2O_4 octahedra also exhibit atomic motion. Due to the ellipsoidal shape of the stress-field regions, the O atoms lying beneath the Ti atoms are moving primarily upward along the

(100) while the O atoms lying beneath the Zr atoms are moving mostly downward.

Tetragonal Response: In this response we report a feature of the stress field not found in any of the other responses for the other materials. Namely, we find oblate regions in the titanate sub-units alternating with prolate regions in the zirconate sub-units. In particular, the responsive regions encompass the entire B metal/oxygen octahedra of their respective sub-units.

IV. DISCUSSIONS

As a general guideline for analysis, it is important to understand the relationship between the ferroelectric distortion direction for a particular material and the direction of uniaxial stress. It is the combination of these effects that will either enhance, diminish or change the nature of the ferroelectric distortion as the stress is applied. We have therefore divided our discussion of the four materials according to this guideline. For all of the above reported responses the direction of uniaxial stress is (100).

In both tetragonal $PbTiO_3$ and the (100)-PZT crystals, the direction of applied stress is parallel to the direction of ferroelectric distortion. Because of this orientation, we have found stress field responses that indicate B metal and oxygen motions along the direction of the uniaxial stress. Application of positive stress moves the atoms from their tetragonal positions towards the paraelectric cubic phase. Since the cubic structure is not ferroelectric, positive stress clearly reduces the ferroelectric distortion; in the way, the local stress field depicts the piezoelectric response of these materials.

For the rhombohedral crystals, the direction of uniaxial stress is not parallel to the direction of ferroelectric distortion. The simplest depiction of this is shown in rhombohedral $PbZrO_3$. It is evident from the tetragonal local stress field that the directions of uniaxial strain and atomic distortion are competitive influences on the B metal and oxygen displacements. Thus, the local stress field depicts two mechanisms for the piezoelectric response: the rotation of the ferroelectric distortion direction from the (100) toward (111) as well as the change in the magnitude of the ferroelectric distortion due to different cation and anion responses.

In the case of (111)-PZT, this competition of influences is more difficult to characterize. Upon uniaxial compression we find no significant motion of the B metal atoms. Instead we find complex Pb and O motions. The origin of O motion deserves particular attention. The motion along (100) and ($\bar{1}$00) of the oxygen atoms that lie directly above and below the B metal atoms can be predicted from either the dilation or tetragonal responses. However, the complex motion of the other oxygen atoms can only be ascertained from a simultaneous analysis of both responses. As an illustration, we examine the motion of the O atom located near ($\frac{1}{4}$,0,$\frac{1}{4}$). Because of its position relative to the expansion region depicted in the dilation response, it has a component of atomic motion along the (001) direction. However, according to the tetragonal response, the same atom also moves along the (0$\bar{1}$0) direction due to the pairing of an oblate response centered in the TiO_6 octahedron and a prolate response centered in the adjacent ZrO_6 octahedron. This same type of analysis can be done for all the oxygen atoms lying equatorial to the B metal atoms and can be used to predict their atomic motions due to uniaxial compression. Based upon these atomic motions, it is possible to characterize the piezoelectric response in (111)-PZT. The piezoelectric response can be summarized as complex motions of the Pb and O sublattices against the almost stationary B metal atomic positions, and not a simple move toward a higher symmetry structure, as seen in the previously described tetragonal crystals.

V. CONCLUSIONS

In this density-functional study, we have examined the induced local stress fields resulting from an externally applied homogeneous uniaxial deformation of two distorted perovskite structures, $PbTiO_3$ and $PbZrO_3$ and the (100) and (111)-PZT superlattices. We have found in the case of materials in which the ferroelectric distortion direction is parallel to the direction of uniaxial stress (tetragonal $PbTiO_3$ and (100)-PZT), the existence of a piezoelectric response involving atomic motions of the B metal and axial O atoms. However, application of stress along a direction not parallel to the ferroelectric distortion directions gives rise to a complicated stress-field pattern (rhombohedral $PbZrO_3$ and (111)-PZT). In particular, we report a piezoelectric response in the rhombohedral $PbZrO_3$ due to B metal and oxygen atomic motions along a composite direction comprised of the (111) atomic distortion and (100) uniaxial strain directions. In the (111)-PZT crystal, we find complex Pb and O motions against a fixed B metal atom sub-lattice upon application of tetragonal stress.

This study demonstrates the utility of stress fields and their applicability to ferroelectric phenomena. The construction of the local stress field is computationally tractable and provides an intuitive way to visualize and understand the response of a crystal to applied stress. Stress-field analyses done in conjunction with spontaneous polarization studies will further broaden the understanding of piezoelectric materials.

ACKNOWLEDGMENTS

We would like to thank Karin Rabe for illuminating and valuable discussions on various aspects of the work. In addition we would like to thank Steven P. Lewis, Eric J. Walter, Lewis D. Book, and Mark Feldstein of the University of Pennsylvania for their help in the preparation of this work and manuscript. We also would like to thank John Shalf of the National Center for Supercomputing Applications for his help with the visualization of the stress fields using AVS 5.02.[27] This work was supported by the Laboratory for Research on the Structure of Matter and the Research Foundation at the University of Pennsylvania as well as NSF grants DMR 93-13047 and DMR 97-02514 and the Petroleum Research Fund of the American Chemical Society (Grant No. 32007-G5). Computational support was provided by the National Center for Supercomputing Applications and the San Diego Supercomputer Center.

[1] J. A. Stroscio and W. J. Kaiser, eds. *Methods of Experimental Physics, Vol. 27* (Academic Press, San Diego, 1993).
[2] B. Jaffe, R. S. Roth and S. Marzullo, *J. Res. Nat. Bur. Stand.* **55**, 239 (1955).
[3] F. Jona and G. Shirane, *Ferroelectric Crystals* (Macmillan, New York, 1962).
[4] T. Ikeda, *Fundamentals of Piezoelectricity* (Oxford, New York, 1990).
[5] Y. Saito, *Jpn. J. Appl. Phys.* **35**, 5168 (1996).
[6] S. Ikegami, I. Ueda and T. Nagata, *J. Acous. Soc. Am.* **50**, 1060 (1971).
[7] E. J. Mele and A. M. Rappe, work in progress.
[8] D. Vanderbilt, unpublished communication (1997).
[9] O. H. Nielsen and R. M. Martin, *Phys. Rev. Lett.* **50**, 697 (1983).
[10] O. H. Nielsen and R. M. Martin, *Phys. Rev. B* **32**, 3780 (1985).
[11] M. C. Payne, M. P. Teter, D. C. Allan, T. A. Arias, and J. D. Joannopoulos, *Rev. Mod. Phys.* **64**, 1045 (1992), and references therein.
[12] A. M. Rappe, K. M. Rabe, E. Kaxiras and J. D. Joannopoulos, *Phys. Rev. B* **41**, 1227 (1990).
[13] L. Kleinman and D. M. Bylander, *Phys. Rev. Lett.* **48**, 1425 (1982).
[14] N. J. Ramer and A. M. Rappe, *Phys. Rev. B*, submitted.
[15] D. D. Koelling and B. N. Harmon, *J. Phys. C* **10**, 3107 (1977).
[16] H. J. Monkhorst and J. D. Pack, *Phys. Rev. B* **13**, 5188 (1976).
[17] H. Fujishita, Y. Shiozaki, N. Achiwa and E. Sawaguchi, *J. Phys. Soc. Jpn.* **51**, 3583 (1982).
[18] H. Fujishita and S. Hoshino, *J. Phys. Soc. Jpn.* **53**, 226 (1984).
[19] S. Teslic and T. Egami, *Acta Cryst. B* submitted, (1997).
[20] R. W. Whatmore and A. M. Glazer, *J. Phys. C* **12**, 1505 (1979).
[21] A. García and D. Vanderbilt, *Phys. Rev. B* **54**, 3817 (1996).
[22] J. D. Friere and R. S. Katiyar, *Phys. Rev. B* **37**, 2074 (1988).
[23] D. Singh, *Phys. Rev. B* **52**, 12559 (1995).
[24] H. Hellmann, *Einführung in die Quanten Theorie* (Deuticke, Leipzig, 1937).
[25] R. P. Feynman, *Phys. Rev.* **56**, 340 (1939).
[26] S. Park and T. R. Shrout, *J. App. Phys.* **82**, 1804 (1997).
[27] AVS 5.02 (Application Visualization System) is a product of Advanced Visual Systems, Inc. of Waltham, Massachusetts.

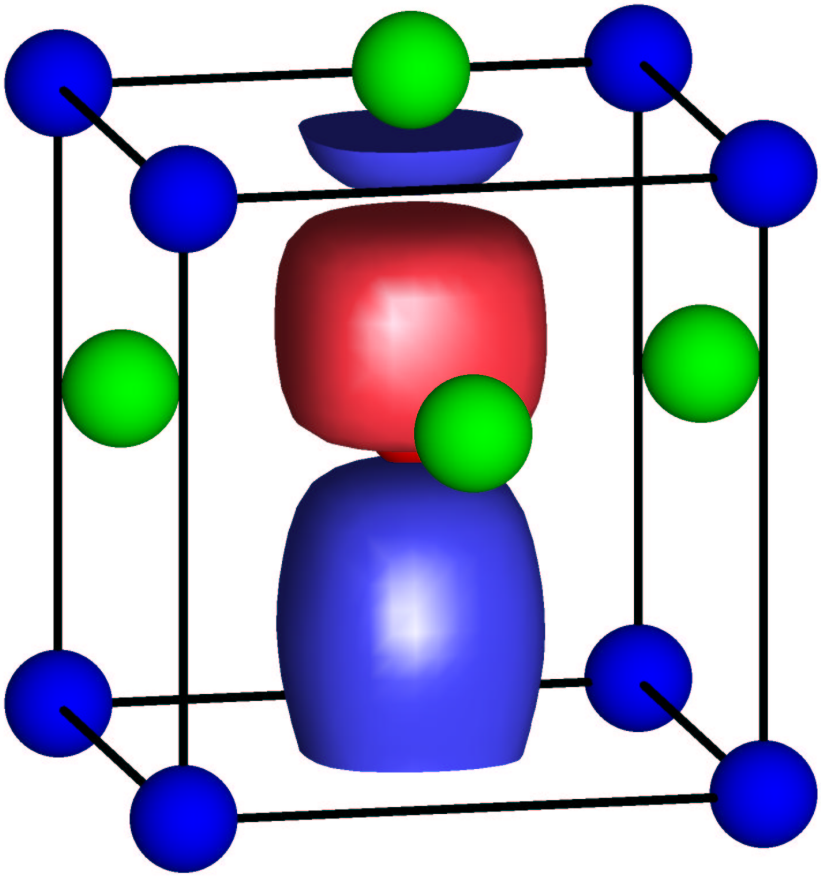

FIG. 1. Tetragonal stress-field response to a uniaxial tetragonal deformation of tetragonal $PbTiO_3$. (blue=lead, red=titanium, green=oxygen).

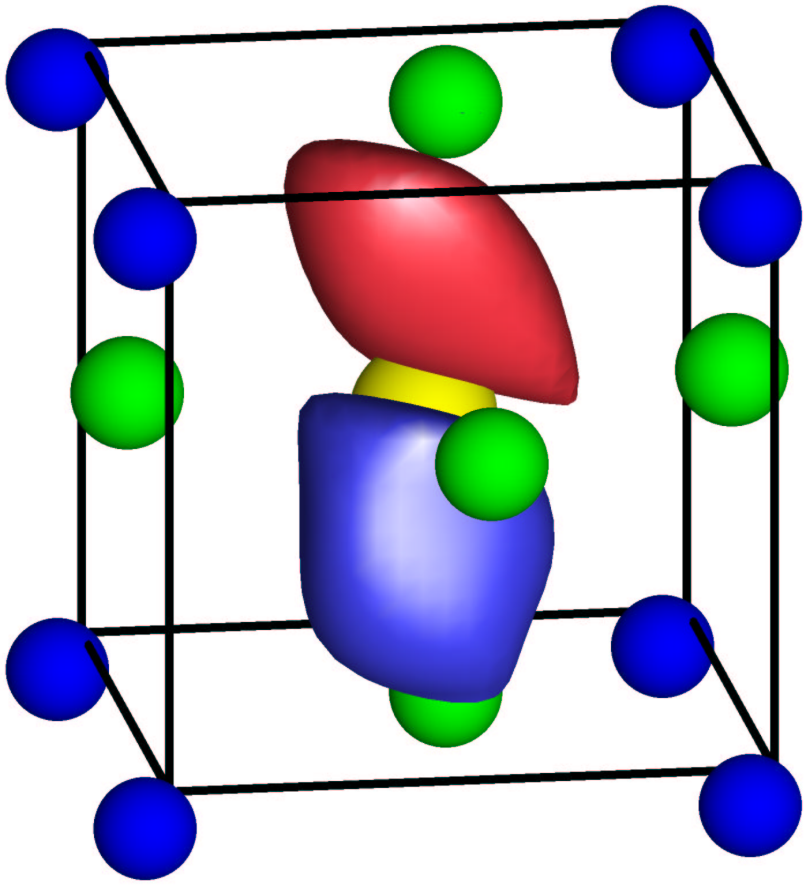

FIG. 2. Tetragonal stress-field response to a uniaxial tetragonal deformation of rhombohedral $PbZrO_3$. (blue=lead, yellow=zirconium, green=oxygen).

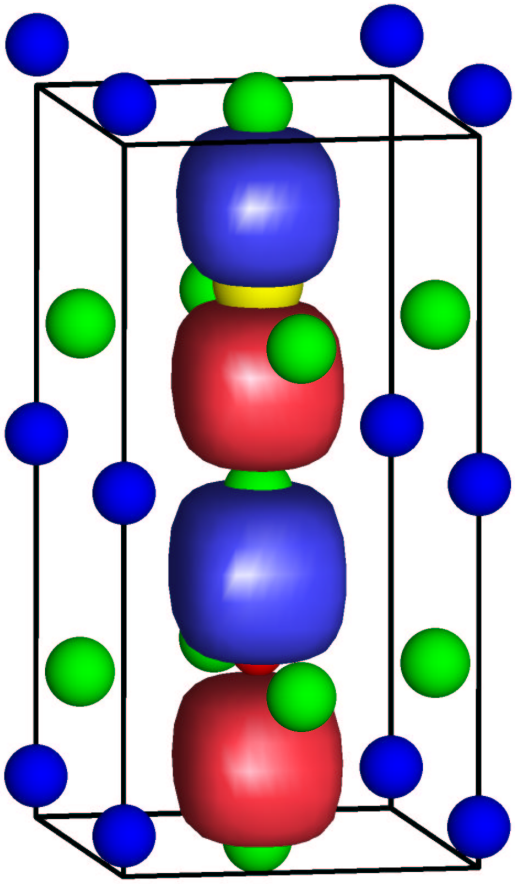

FIG. 3. Tetragonal stress-field response to a uniaxial tetragonal deformation of tetragonal (100)-Pb($Zr_{0.5}Ti_{0.5}$)O_3. (blue=lead, yellow=zirconium, red=titanium, green=oxygen).

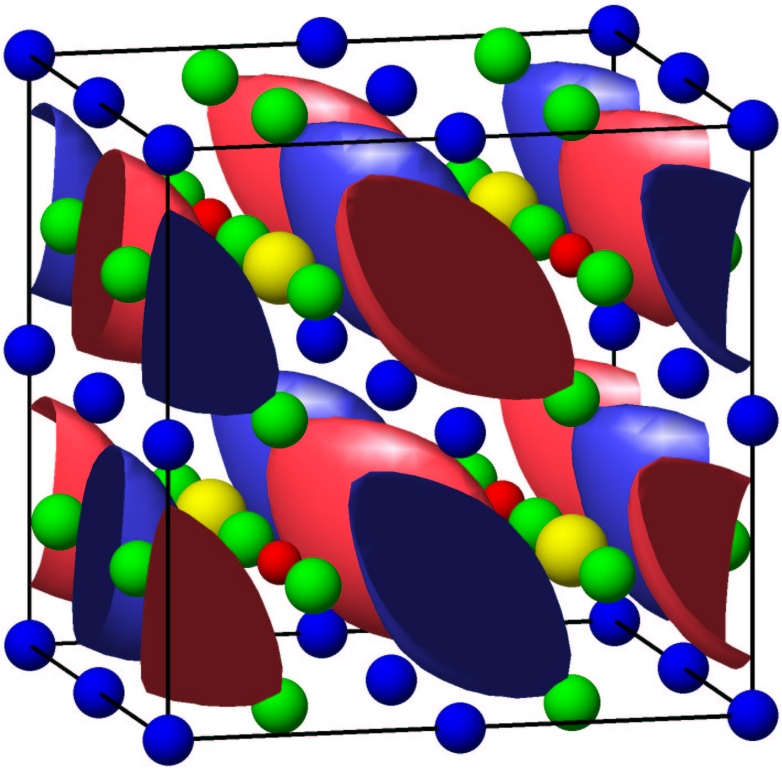

FIG. 4. Dilation stress-field response to a uniaxial tetragonal deformation of rhombohedral (111)-Pb($Zr_{0.5}Ti_{0.5}$)O_3. (blue=lead, yellow=zirconium, red=titanium, green=oxygen).

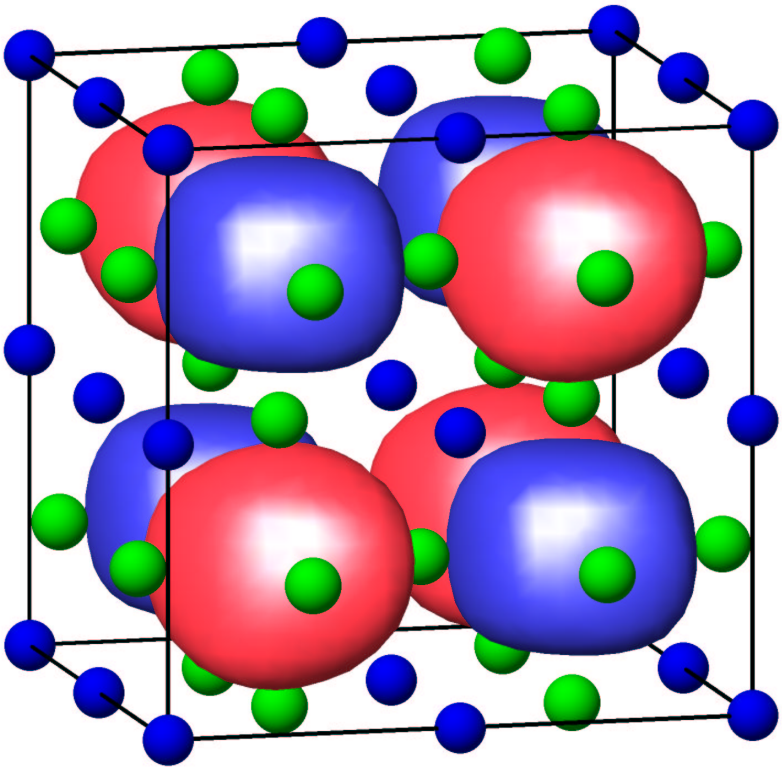

FIG. 5. Tetragonal stress-field response to a uniaxial tetragonal deformation of rhombohedral (111)-Pb($Zr_{0.5}Ti_{0.5}$)O_3.